




Au-sensitized ZnO nanostructures for efficient photoelectrochemical splitting of water

Ebrima L. Darboe¹, Sayed A. S. Mosamem¹, Shruti Shah¹, Vidhika Sharma¹, Bharat Bade¹, Swati Rahane¹, Vidya Doiphode¹, Pratibha Shinde¹, Ashish Waghmare¹, Yogesh Hase¹, Ashvini Punde¹, Somnath Ladhane¹, Mohit Prasad^{1,2,*}, and Sandesh Jadkar^{1,*} 

¹ Department of Physics, Savitribai Phule Pune University, Pune 411 007, India

² Department of Applied Science and Humanities, Pimpri Chinchwad College of Engineering, Nigdi, Pune 411 004, India

Received: 27 April 2023

Accepted: 27 November 2023

Published online:
13 December 2023

© The Author(s), under exclusive licence to Springer Science+Business Media, LLC, part of Springer Nature, 2023

ABSTRACT

In this study, different structures of ZnO, such as nanorods (NR), nanosheets (NS), nanowires (NW), and nanospheres (NSP), were synthesized and then sensitized with Au plasmons for efficient photoelectrochemical splitting of water. The electrodeposition method was used to realize different ZnO nanostructures and decorate them with Au nanoparticles. X-ray diffraction (XRD) confirms the hexagonal wurtzite structure of ZnO photoanodes, and the average crystal size was ~ 30 nm. The morphology of ZnO nanostructures depends on the concentration of Zn(NO₃)₂ · 6H₂O, and a variation in it leads to the evolution of nanorods, nanosheets, nanowires, and nanospheres. UV–visible and photoluminescence (PL) spectroscopy give the bandgap value (~ 3.1 eV) and good absorption in the visible region on decoration with Au plasmons. The photoelectrochemical (PEC) splitting of water experiment results indicate that the photoanode of ZnO-NS (0.05 M) loaded with Au plasmons-based photoanode has better performance with 0.38% efficiency and a photocurrent density of 0.68 mA/cm². Different ZnO photoanodes can be designed and constructed containing various types of ZnO morphology for efficient PEC water splitting, as evident from the preliminary results.

1 Introduction

The rapid depletion of primary energy sources and their environmental impact demand research for sustainable, green, and clean energy sources [1]. Photoelectrochemical (PEC) splitting of water is a promising way for sustainable energy production. Hydrogen is a clean and green gas, without any pollution or environmental hazard compared to nonrenewable energy

sources, which causes global climate change due to greenhouse gas emissions [2]. Metal oxide composites with plasmons have attracted wide interest in photoelectrochemical (PEC) splitting of water [3]. Many metal oxides with Au and Ag plasmons have been probed for this purpose [4]. The first metal oxide investigated for water splitting using PEC cells was TiO₂, carried out by Fujishima et al. [5]. The metal oxide candidates can provide enough energy (~ 1.23 eV) in the

Address correspondence to E-mail: mohitprasad7@gmail.com; sandesh@physics.unipune.ac.in

presence of light to drive the water-splitting reaction [6, 7]. ZnO has similar properties to TiO₂ as band edge, and bandgap positions are almost the same [8]. ZnO, a direct bandgap material (~ 3.3 eV) with high electron mobility, is a potential candidate for PEC applications [9]. However, due to its large bandgap, the absorption range of light is not in the visible region [10]. Plasmons are remarkably utilized to shift the absorption range into the visible region [11]. On the other hand, different structures of the nanoparticles, such as nanorods, nanospheres, nanoflowers, nanosheets, and nanowires, of ZnO can exhibit different properties for efficient harvesting of light.

The performance of the PEC cell is dependent on the properties of the synthesized photoelectrodes. Hence, various materials have been investigated to increase PEC cell efficiency [12]. Metal oxide semiconductors are under the scope of researchers due to their inexpensive and scalable nature for hydrogen production [13]. It has been realized that metal oxide with plasmons is better for PEC activity as plasmons enhance charge transfer and inhibit charge recombination [3]. Many researchers have worked on metal oxides with noble metals for PEC water-splitting applications with various configurations. Some recent studies which have shown promising results are enlisted as follows. The effect of plasmonic nanoparticles and surface passivation on ZnO nanostructures was studied by Liu et al. [14], who reported 6.7 times higher efficiency than pristine ZnO. Prasad et al. [15] have reported that Z-NRs-Ag has better optical absorption than Ag-Z-NRs. Hongxia Li et al. [16] reported that surface plasmon resonance enhances the PEC performance of the TiO₂-Au system. Mahala et al. [17] studied the near-field–far-field effects of Au plasmons on ZnO nanostructures, having a maximum efficiency of 0.514% compared to bare ZnO. Zayed et al. [18] studied the morphological effect of ZnO/Au nanostructures with ABPE ~ 2.05%. Saboor et al. [19] reported that the ZnO-NR modified with Au (deposition time 60 s) exhibited a photocurrent density ~ 660 $\mu\text{A}/\text{cm}^2$ at a bias of 1.0 V/SCE. Li et al. [20] reported that the ZnO@TiO₂ (15 nm)/Au (8 nm) array shows the maximum photocurrent density of 3.14 mA/cm^2 at 1.2 V vs. RHE.

In this study, the PEC properties of different structures (nanorods, nanosheets, nanowires, and nanospheres) of ZnO loaded with Au plasmons are compared with their bare counterparts. Au nanoparticles (NPs) are used as the plasmonic layer because of their wide range of light absorption, i. e., visible

light absorption and UV light absorption (due to the transition from 5d to 6sp electronic inter-band), and they also prevent corrosion during the photoreaction [21]. ZnO nanostructures are deposited on the FTO substrate, and then the Au nanoparticles (NPs) i.e., Au plasmons, are deposited on top of ZnO nanostructures using the electrodeposition technique. This technique is beneficial for depositing different nanostructures of ZnO on FTO substrate at a low cost and maintains purity in the synthesized samples [22, 23]. Herein, Au-ZnO nanostructures synthesized via the one-step electrodeposition method are proposed as photoanodes, which have a high surface area with enhanced photocurrent response compared to previously reported data [24–28]. These findings reveal the significant importance of the Au-ZnO-based nanosheets for application in PEC cells and energy conversion devices.

2 Experimental

2.1 Materials and methods

The electrodeposition method was based on a typical three-electrode system for depositing ZnO-nanostructured thin films with different morphologies, and Au NPs were deposited on top of them. The substrate was a conducting-coated glass substrate i.e., FTO substrate. The utilized electrodes i.e., (reference electrode and counter electrode) were saturated calomel electrode (SCE) and Pt mesh, respectively. The immersed substrate in the solution is the working electrode. Before deposition, all the substrates were cleaned with three different kinds of liquid (acetone, ethanol, and water) sequentially for 5 min using the ultrasonication method. To obtain ZnO nanostructures, i.e., nanorods (NR), nanowires (NW), nanosheets (NS), and nanospheres (NSP) morphologies, aqueous solutions of Zn (NO₃)₂·6H₂O with different concentrations of 0.001 M, 0.01 M, 0.05 M, and 0.1 M were used. The concentration of KCl was kept at 100 mM. The bath containing this solution was held at 85 °C, and the applied step potentials were -1.1 for 3600 (nanosheets and nanospheres) and 7200 s (nanorods and nanowires), respectively. The pH value of the precursor solution was around ~ 8 during the preparation of all the samples. After the deposition process, the synthesized thin films were cleaned with distilled water and subsequently dried at room temperature. These thin films were further annealed at 400 °C in a muffle furnace.

To deposit Au nanoparticles on the top of ZnO synthesized films, a solution of HAuCl_4 with 0.6 mM concentration and 50 mM NaNO_3 was used for a 100 s duration with an applied potential of -0.4 V/SCE. The synthesized thin films were rinsed with distilled water and then dried for 1 h in the oven at 100 °C.

2.2 Characterizations and apparatus

XRD patterns were recorded in the range of 20 – 80° using Bruker D8 to recognize the crystal structure of the synthesized thin films. Further, SEM was carried out using JEOL JSM630A to visualize the surface morphologies and to determine the mean size of particles. UV–Visible absorption spectra were recorded to determine photoanode bandgaps using a JASCO V-670 spectrophotometer and PL using a Horiba Fluorolog spectrometer to indicate the absorption bands associated with each morphology with Au and without Au NPs. PEC properties of the synthesized photoanodes were investigated using photocurrent (J – V), electrochemical impedance spectroscopy (EIS), and Mott–Schottky (MS) analysis. MS and EIS were recorded using the same potentiostat to obtain the flat band potentials, charge carrier densities, and the lifetime of photogenerated charge carriers. J – V characteristics were recorded using a potentiostat (Metrohm Autolab PGSTAT302N) and a 150 W Xenon Lamp (PEC-L01) with a light intensity of 100 mW/cm² (AM 1.5). Three electrode glass reactor was utilized to investigate the photoelectrochemical behavior of the synthesized photoanodes. In the cell, three electrodes were used: a saturated calomel electrode, a platinum foil counter electrode, and a ZnO-based photoanode as the reference electrode (SCE), counter electrode (CE), and working electrode (WE), respectively. 0.5 M Na_2SO_4 solution was used as an electrolyte. The size of the working electrode was ~ 1 cm², and the sheet resistance of FTO was ~ 7 Ω/. The experimental work was done with AR-grade chemicals and double-distilled deionized water.

3 Results and discussion

3.1 X-ray diffraction (XRD) analysis

XRD analysis was carried out to obtain the crystallographic information [29]. Figure 1 shows the XRD pattern of all the synthesized photoanodes in the

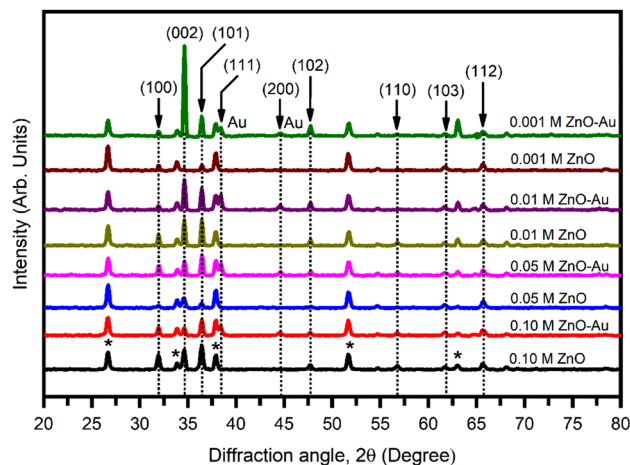


Fig. 1 XRD pattern for ZnO-nanospheres, nanosheets, nanowires, and nanorods with and without loaded Au plasmons on the top

range of 20° – 80° for 2θ . The diffraction peaks of the FTO were marked with an asterisk (*), and the gold with its chemical symbol. The multiple peaks at $2\theta \sim 31.7^\circ$, 34.4° , 36.4° , and 47.5° can be well indexed to (100), (002), (101), and (102) lattice planes of ZnO hexagonal wurtzite structure having lattice constants $a = b = 3.28$ Å and $c = 5.25$ Å (JCPDS, file no 36-1451) [30, 31]. It indicates that the ZnO nanostructures had grown on the FTO substrate successfully. The sharp and intense ZnO peaks illustrate the sample high crystallinity. The observed peaks at 38.3° and 44.4° can be assigned to the (111) and (200) planes of Au, indicating face-centered cubic (FCC) bravis lattice type with lattice constant 4.2 Å (JCPDS, file no 04-784), confirming the presence of Au plasmons on the top of ZnO. The plane (002) shows the highest intensity for ZnO–Au nanorods establishing their preferred direction along the c -axis. The nanosheets are randomly oriented, thus showing 2D planar orientation with the plane present (101). The structural parameters of all the concentrations varied, and plasmons decorated ZnO films were calculated by the *Williamson–Hall* method.

The crystallite size (D) was estimated by *Debye–Scherrer’s* equation [32],

$$D = \frac{K \lambda}{\beta \cos \theta}, \quad (1)$$

where D is the average crystallite size, λ is the x-ray wavelength (Cu- $K\alpha$, $\lambda = 1.54056$ Å), θ is the Bragg angle in radians, and K is the Scherrer constant (0.94). K depends on the crystallite shape and the size

distribution, indices of the diffraction line [33]. β is the full width at half maximum (FWHM) in radians correction of instrumental broadening effect. The broadening of the diffraction peak is due to defects present in the material and instrumental errors, which become additive [34]. The residual strain in the crystallite disturbs the crystal lattice, which causes the diffraction peaks to broaden. In such circumstances, *Williamson Hall's* analysis [35] should be applied using Eq. (1) by the following equation.

$$\beta \cos \theta = \frac{K \lambda}{D} + 4 \epsilon \sin \theta \quad (2)$$

It represents a linear equation with $K\lambda/D$ as the intercept. By plotting a graph of $\beta \cos \theta$ vs. $4 \sin \theta$, one can find the slope and also the microstrain. The slope is inversely proportional to the crystal size (D), and the intercept is termed microstrain. These plots are known as Williamson–Hall ($W-H$) plots. Figure 2 represents the $W-H$ plots for each concentration variation for pristine ZnO nanostructures and Au-decorated ZnO-nanostructured film.

Estimated values of crystal size (D) and microstrain (ϵ) of all the variations are listed in Table 1.

Au plasmons are deposited on the ZnO film, which might change the interfacial interaction, potentially leading to crystal size and microstrain modifications. Also, Au sensitization could induce stress in the ZnO film due to lattice mismatch between Au and ZnO followed by strain relaxation in ZnO to adjust the accommodated Au plasmons. The atomic radius of Au is larger than Zn; thus, some structural changes may occur after Au sensitization [36]. The strain in the films is compressive ($\epsilon < 0$) at the initial stage of the ZnO film formation and tends to be tensile ($\epsilon > 0$) after Au plasmon incorporation [37].

3.2 Scanning electron microscopy (SEM) analysis

SEM analysis was carried out to reveal the surface morphology of the samples. Figure 3 depicts the top-view SEM images of the ZnO nanostructures. The basic parameters of the various structures of ZnO thin films were calculated using *Image j software*. The average diameter and the length of vertically aligned ZnO nanorods on the FTO substrate were ~ 380 nm and ~ 1391 nm, respectively (Fig. 3a1). The diameter of nanowires and the width of nanosheets were estimated and were ~ 102 nm and ~ 426 nm, respectively

(Fig. 3b1). As the $\text{Zn}(\text{NO}_3)_2 \cdot 6\text{H}_2\text{O}$ concentration changes, the morphology shifts from nanospheres to nanorods. It indicates the direct dependence of morphology on $\text{Zn}(\text{NO}_3)_2 \cdot 6\text{H}_2\text{O}$ concentration. It can be seen that the different concentration of precursor has led to different morphologies of the ZnO nanostructures formation on the FTO substrate. Nanospheres, nanosheets, nanowires, and nanorods were formed from the 0.1 M (Fig. 3a1), 0.05 M (Fig. 3b1), 0.01 M (Fig. 3c1), and 0.001 M (Fig. 3d1) concentrations of $\text{Zn}(\text{NO}_3)_2 \cdot 6\text{H}_2\text{O}$, respectively. Moreover, the average size of Au NPs is a few nm and uniformly dispersed all over the film (Fig. 3a2–d2). In our study, we observed that the average size of Au NPs in our case is bigger than previously reported results [18]. As reported earlier, the light scattering phenomenon dominates in larger-size nanoparticles as optimum scattering occurs. In addition, surface plasmons resonance can also occur by far-field scattering, i.e., (radiative process) for large-size nanoparticles [17].

3.3 Photoluminescence (PL) analysis

PL analysis was further used to determine the bandgap type, estimate the recombination rate, and calculate the material's charge transfer and defect density. The laser beam with a wavelength of 350 nm was used as the excitation wavelength in this process. Figure 4 shows the PL emission spectrum of the synthesized photoanodes in the visible region.

The obtained spectrum indicates that the bandgap of the material is direct. Indirect bandgap materials do not possess luminescence but thermally lose their energy by phonon emission. All the synthesized samples had almost the same peak at 388 nm with different intensities, attributed to the radiative recombination of charge carriers. Figure 4 shows an additional emission band in the visible region related to the recombination of photoexcited holes and electrons of oxygen vacancies and the defect state on the surface of ZnO [38]. It corresponds to the bandgap of ZnO thin films. The emission intensities are improved for all ZnO-nanostructured films loaded with Au. The improvement in the intensities of Au-decorated ZnO can be due to the emission of hot electrons from the Au NPs. The weakened intensity of pristine ZnO is due to oxygen vacancies, which decrease deep-level emission [39]. The highest intensity peak is observed for the nanosheet structure. The defects present in the materials act as non-radiative recombination sites. The

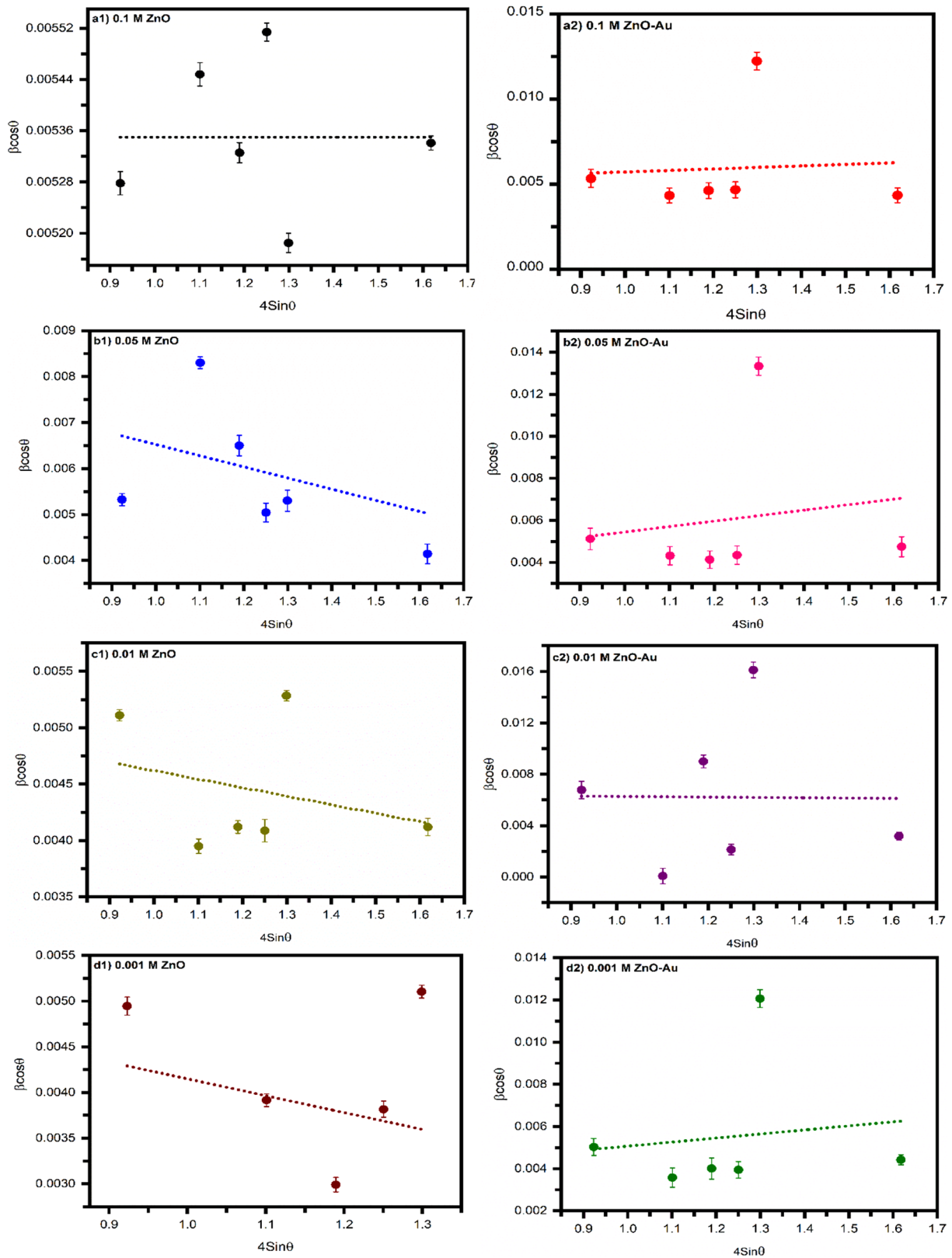


Fig. 2 $W-H$ plots for bare ZnO-nanospheres, nanosheets, nanorods, and nanowires and with Au plasmons loaded on top

Table 1 Values of crystal size (D) and microstrain (ϵ) for each concentration

Concentration	Crystal size (D) nm	Micro strain (ϵ) $\times 10^{-3}$
0.1 M ZnO	26	-4.37
0.1 M ZnO–Au	22	0.88
0.05 M ZnO	14	-3.30
0.05 M ZnO–Au	41	2.00
0.01 M ZnO	26	-0.75
0.01 M ZnO–Au	21	0.84
0.001 M ZnO	25	-1.20
0.001 M ZnO–Au	41	1.70

irregularity in grain size is responsible for the change in emission intensity. It indicates the low defect density of synthesized material.

3.4 UV–Visible spectroscopy

UV–Visible spectroscopy was carried out to determine the optical properties of the synthesized films [40]. Figure 5a shows the corresponding recorded absorption spectra. The optical band gap is calculated from the Tauc plot equation as,

$$(\alpha E)^{\frac{1}{n}} = B^{\frac{1}{n}} (E - E_g), \quad (3)$$

where α is the absorption coefficient, E indicates the incident photon energy, B indicates the optical density of states, E_g is the optical band gap, and n takes different values corresponding to different transitions. It takes values such as $1/2$, $3/2$, 2 , and 3 for direct allowed, direct forbidden, indirect allowed, and indirect forbidden energy states, respectively. An optical band gap is obtained by extrapolating the tangential line to the photon energy in $(\alpha E)^{1/2}$ as a function of the E plot (Tauc plot). The pristine ZnO-nanostructured thin films exhibited sharp absorption bands at around 384 nm for all different structures, indicating a bandgap of 3.23 eV [41]. The obtained bandgap is slightly lower than the previously reported value (3.4 eV), giving intense absorption in the visible region. However, the absorption may be controlled by intermediate defect states. Despite the same absorption point, the intensity of absorptions is different for different structures. It shows the dependence of the trapping of light on the type of morphology. Figure 5b illustrates

the band edge positions and direct bandgap nature of ZnO. ZnO-nanostructured films with Au plasmons exhibited sharp absorption bands for the 0.1 M, 0.05 M, 0.01 M, and 0.001 M concentrations, showing bandgaps 3.16 eV, 3.15 eV, 3.14 eV, and 3.18 eV, respectively (Fig. 5b).

The reduction in the bandgap of ZnO nanostructures loaded with Au plasmons could be due to metal interaction with incident light, followed by intense absorption in the visible range. As Au plasmons are incorporated for light absorption, the absorption edge is red-shifted toward the visible region, improving the absorption rate [20]. The shift in the absorption band from pristine ZnO is attributed to the decoration of Au plasmons that alters the band positions. The highest absorption was observed for 0.1 M pristine ZnO, followed by 0.05 M ZnO–Au in the visible region. The absorption spectra plot indicates that adding Au NPs causes a red shift for all combinations. It is caused by the surface plasmon resonance effect, which stimulates light and gold nanoparticle interaction [42]. The excited surface plasmons produced by the Au nanoparticles vibrate the matrix surrounding them, increasing the near-field amplitude and improving visible light absorption. The band gap of Au–ZnO decreases to 3.1 eV upon loading of Au NPs. The simultaneous effect of surface plasmon resonance and the size of nanosheets in the ZnO–Au system led to increased visible light absorption. Thus, the morphology of nanostructures is in proper agreement with the absorption spectra [17].

3.5 Photoelectrochemical performance

The linear sweep voltammetry (LSV) method was used to determine the PEC water splitting properties of the photoanodes using three electrodes at -1.0 to 1.0 V vs. SCE with the scan rate of 20 mV/s in 0.5 M Na₂SO₄ electrolyte.

3.5.1 Photocurrent measurement

The J – V characteristics were measured under light illumination in the visible region (Fig. 6). A small dark current for all photoanodes, including pristine and Au-loaded ZnOs, was observed, indicating a non-faradic reaction [19].

After illumination, a sharp rise in photocurrent was observed. As the photons are incident, the

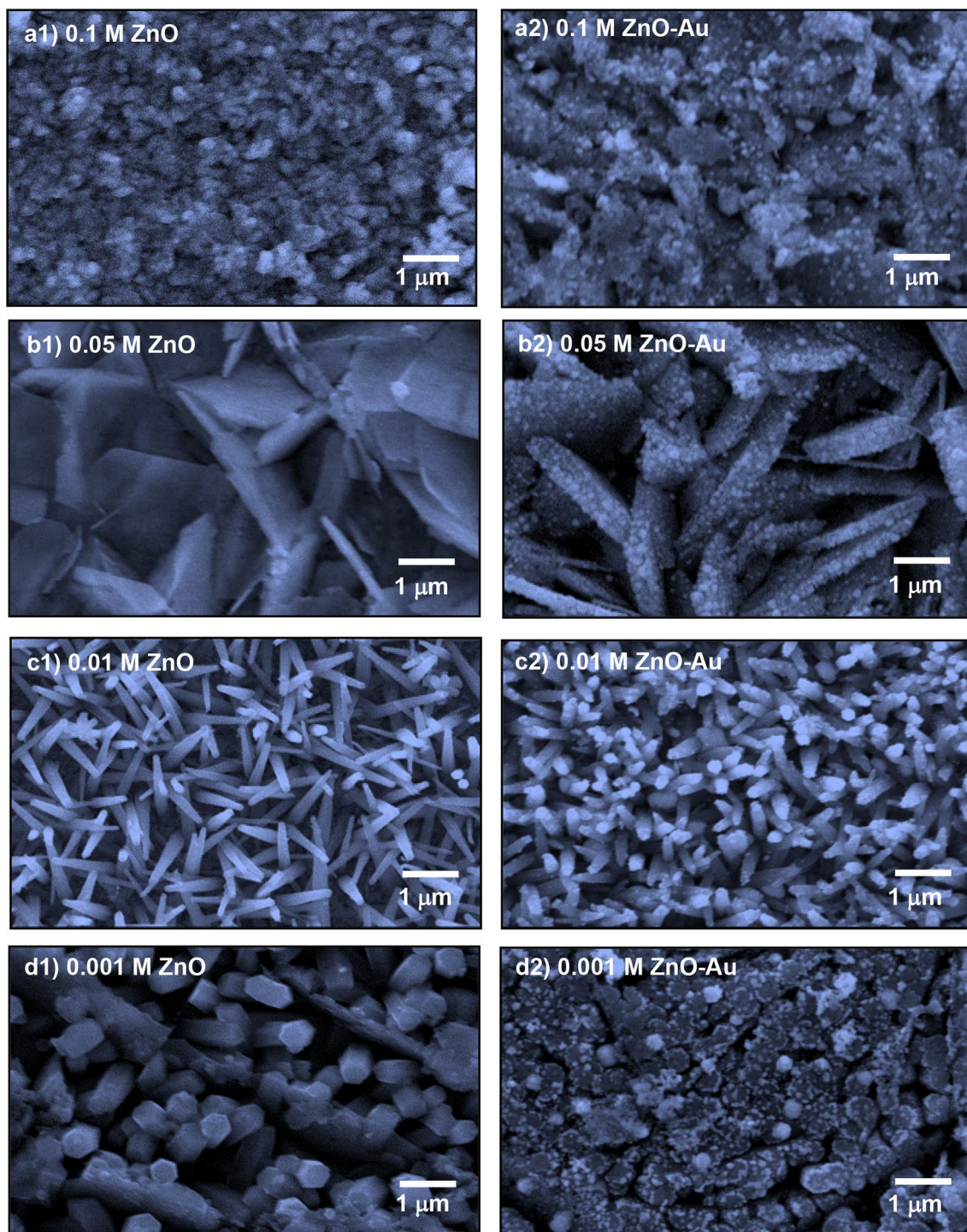


Fig. 3 Top view of the SEM images of different structures of pristine ZnO and ZnO coated with Au plasmons

electron–hole pairs are generated, and these electron–hole pairs separate, and the electrons travel to the counter electrode, where the reduction of protons produces H_2 , and the holes react with H_2O (water

molecules) to evolve O_2 . The measured photocurrents at 1 V applied potential are listed in Table 2.

The largest photocurrent was observed for the 0.05 M ZnO–Au and the smallest for the 0.001 M

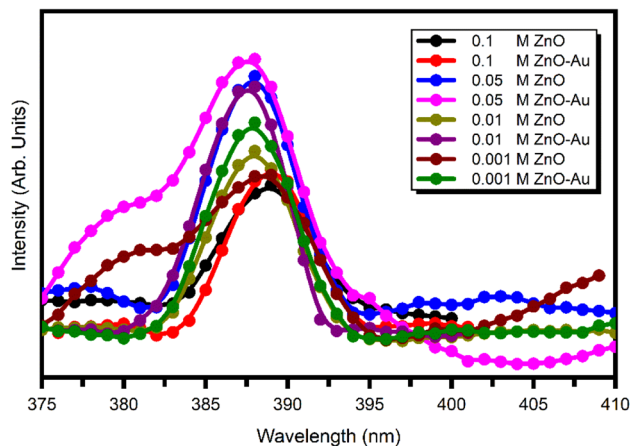


Fig. 4 Photoluminescence (PL) spectrum of pristine ZnO thin films and Au-loaded ZnO thin films

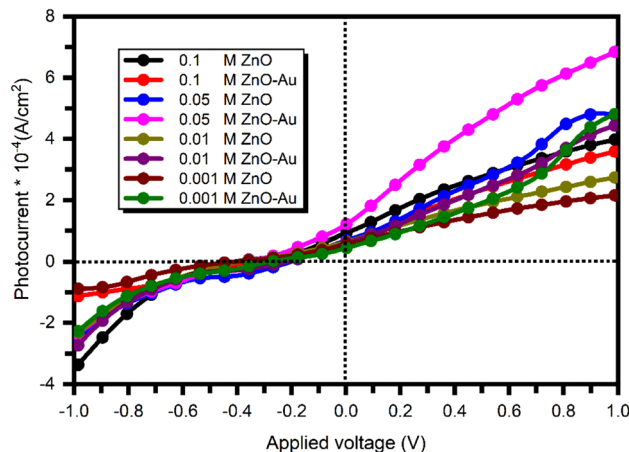


Fig. 6 The *J*–*V* characteristics of all synthesized photoanodes

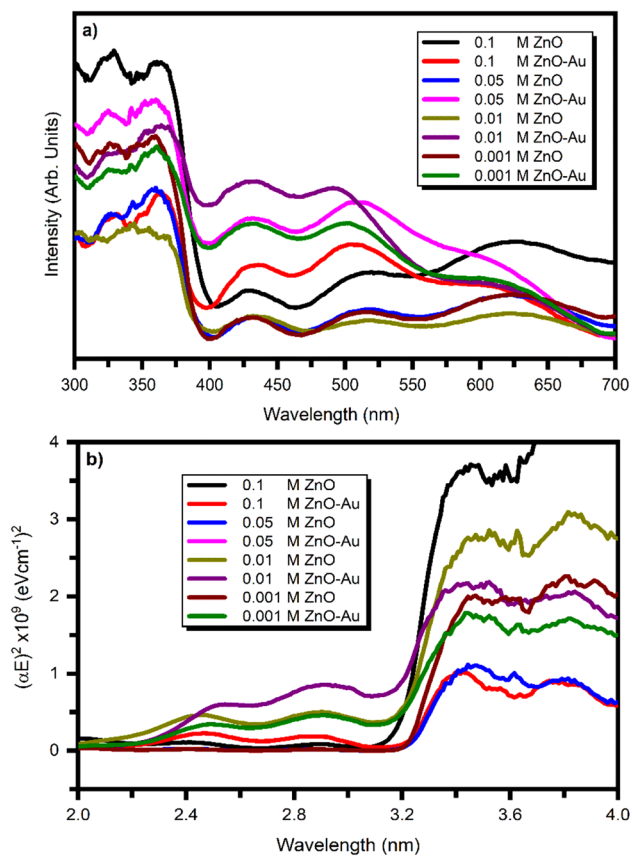


Fig. 5 The UV–Visible spectra of ZnO nanostructures and ZnO/Au nanostructures. **a** Absorption spectra, **b** Tauc plot

ZnO configured photoanodes. The nanospheres (0.1 M ZnO) and the nanosheets (0.05 M ZnO) are two morphologies with better photocurrent density

Table 2 Photocurrent densities at 1 V applied potential and maximum photon-to-hydrogen efficiency (η_{\max}) for all configured photoanodes

Photoanode	Photocurrent density at 1 V(A/cm ²)	(ABPE) (%)
0.1 M ZnO	3.61×10^{-4}	0.17
0.1 M ZnO–Au	4.48×10^{-4}	0.20
0.05 M ZnO	3.98×10^{-4}	0.21
0.05 M ZnO–Au	6.87×10^{-4}	0.38
0.01 M ZnO	2.75×10^{-4}	0.14
0.01 M ZnO–Au	4.39×10^{-4}	0.17
0.001 M ZnO	2.14×10^{-4}	0.11
0.001 M ZnO–Au	4.82×10^{-4}	0.16

performance. The Au plasmonic layer boosts photocurrent density because the confined plasmonic effect of Au clusters on the top of Au–ZnO enhances localized field strength, increasing the light absorption coefficient. The study shows that light is absorbed by Au plasmons, which then produce hot electrons. The photocurrent density increases due to the hot electrons insertion into the ZnO conduction band and subsequent drift toward the cathode [43, 44]. Au nanoparticles can capture the photoinduced electrons of ZnO–NRs because their Fermi levels are lower than the CB of ZnO–NRs, which prevents charge recombination. The photoanodes absorb photons and produce e[–]–h⁺ pairs when illuminated with UV–Visible light. In contrast to the photogenerated h⁺, which will remain on the VB of ZnO–NRs, the e[–] on the VB of ZnO–NRs will be stimulated to the CB of ZnO–NRs. The excited e[–] produced in ZnO–NRs

is transferred to Au NPs, resulting in the effective separation of charge carriers produced by light. The direct transfer of photogenerated charges from ZnO-NRs to Au NPs is made possible by the close contact of Au nanoparticles with the ZnO-NRs. Additionally, this mechanism is expected to prevent charge recombination between the e⁻ in the semiconductor material and the h⁺ in the gold nanoparticles. The metal–semiconductor interface is where the Schottky barrier displays the same behavior. The method described here emphasizes the importance of Au NPs in boosting ZnO-NRs PEC characteristics. Compared to other Au-ZnO nanostructures, Au-sensitized ZnO nanosheets had higher photocurrent densities. It is because of the larger surface area, which allows for more light absorption in a wider wavelength range. Therefore, compared to bare ZnO-NRs samples and other Au-ZnO nanostructures synthesized photoanodes, the Au-ZnO nanosheets-based photoanode exhibits synergism of the utmost importance, resulting in an improved PEC activity. In this way, Au NPs affect photocurrent density promotion. An increase in photocurrent is there because more light is captivated by the material, which causes a sharp rise in the absorption. The results obtained are in good agreement with the optical characteristics. The applied bias to-photon-conversion efficiency (ABPE) of the configured photoanodes was estimated using the following equation [15, 45],

$$ABPE(\%) = \frac{J_{ph}(1.23 - |V_{Bias}|)}{P_{Light}} \quad (4)$$

where J_{ph} is the photocurrent density in mA/cm², V_{Bias} is the applied external bias in Volt, and P_{Light} is the power density of incident light irradiance in mW/cm², which was around 100 mW/cm².

Figure 7 shows the η_c plot of all the photoanodes in the 0–1.0 V applied potential range. The maximum efficiencies were obtained for the 0.1 M ZnO modified with Au plasmons. The values are listed in Table 2.

As the Au NPs are incorporated, the photocurrent density and efficiency values vary considerably. For instance, η_c (max) is 0.21% for the pristine ZnO with 0.05 M concentration, whereas it increases to 0.38% for the modified 0.05 M ZnO with Au. The conversion efficiency is a function of the concentration of synthesized material on the FTO substrate, and the type of structure evolved.

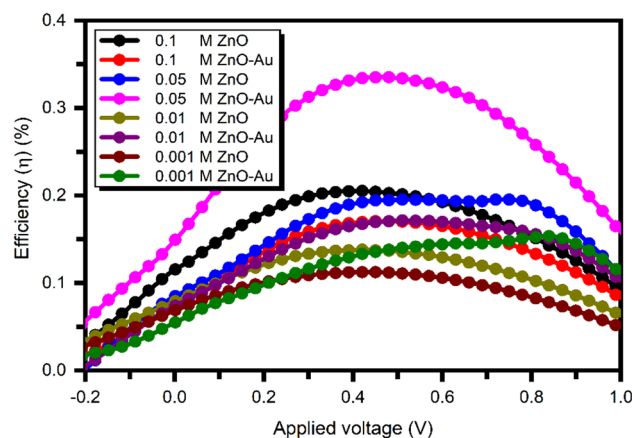


Fig. 7 Photoconversion efficiency of all synthesized photoanodes

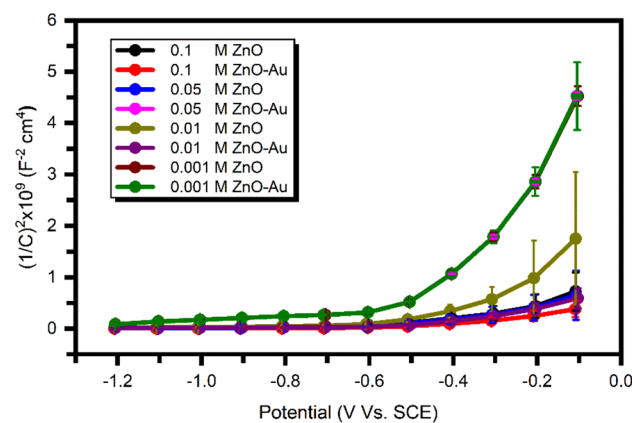


Fig. 8 Mott–Schottky plot of all synthesized photoanodes

3.5.2 Mott–Schottky analysis

Mott–Schottky was used to deduce the fundamental properties of the synthesized photoanodes, such as flat band potential (V_{FB}), donor density (N_d), and depletion layer width (ω). Figure 8 shows the Mott–Schottky plot of all configured photoanodes.

The capacitance was calculated based on electrochemical impedance spectroscopy (EIS) data associated with different potentials in the dark at 500 Hz frequency. The parameters were obtained using the Mott–Schottky equation, which is given by,

$$\frac{1}{C^2} = \left(\frac{2}{e\epsilon_0\epsilon N_d A^2} \right) \left(V - V_{FB} - \frac{KT}{e} \right) \quad (5)$$

where C is the capacitance of the depletion region at applied potential V , e is the fundamental charge, ϵ_0

is the permittivity of the vacuum, ϵ is the dielectric constant of the material, which is 8.5 for ZnO [46, 47], N_d is the donor density, V_{FB} is flat band potential, and KT/e is a temperature-dependent correction term which is around 0.025 V.

The flat band potential (V_{FB}) was obtained by extrapolating the linear portion of the Mott–Schottky plots to the x-axis intercepts. The obtained results are shown in Table 3. For any photoanode, the absolute value of flat band potential for the ZnO modified with Au is greater than its pristine form. The values range from -0.43 V to -0.47 V. The free charge carrier concentration N_d was calculated from the slope value of the linear portion of the plots using the modified Mott–Schottky equation [48],

$$N_d = \frac{2}{e\epsilon_0\epsilon A^2(\text{slope})} \quad (6)$$

A^2 has already been added to the slope dimension. All the pristine samples indicate that the donor density is of the order of $\sim 10^{21} \text{ cm}^{-3}$, whereas it was $\sim 10^{22} \text{ cm}^{-3}$ for the samples modified with Au. The most significant donor densities were obtained for the pristine 0.05 M ZnO, and the sample was modified with Au plasmons (Table 3).

The width of depletion layers was calculated by considering 1 V applied potential to the working electrode, and the values for the V_{FB} and N_d are obtained using the following equation [49],

$$w = \left(\frac{2\epsilon_0\epsilon(V - V_{FB})}{e_0N_d} \right)^{\frac{1}{2}} \quad (7)$$

The smallest space charge layer was found for the pristine 0.05 M ZnO and its modified form with Au, as it has an inverse relation with donor density N_d (Table 3).

Table 3 Donor density, flat band potential, and depletion layer width estimated at 1 V applied potential for the synthesized photoanodes

Photoanode	Donor density (cm^{-3})	Flat band potential (Volt)	Depletion layer width (nm)
0.1 M ZnO	7.72×10^{21}	-0.43	0.26
0.1 M ZnO–Au	1.49×10^{22}	-0.45	0.19
0.05 M ZnO	8.85×10^{21}	-0.45	0.24
0.05 M ZnO–Au	3.27×10^{22}	-0.48	0.12
0.01 M ZnO	2.86×10^{21}	-0.40	0.44
0.01 M ZnO–Au	9.65×10^{21}	-0.44	0.23
0.001 M ZnO	1.23×10^{21}	-0.43	0.66
0.001 M ZnO–Au	1.22×10^{21}	-0.43	0.66

3.5.3 Electrochemical impedance spectroscopy (EIS)

EIS was carried out to calculate the lifetime of the photogenerated electron–hole pairs, interfacial charge migration, and interfacial resistance. The resistance while transporting the electron for smaller semicircle is low. It highlights the charge carrier separation rate [50]. Figure 9 illustrates the result of the EIS measurements for the synthesized photoanodes.

The smaller arc diameter expresses the forceful dissociation of the photogenerated electron–hole pairs and the expeditious interfacial charge-shifting operation [15]. The larger arc diameter indicates a shorter lifetime than the smaller arc diameters, which can be assigned to a prolonged lifetime [14, 19]. The 0.05 M ZnO–Au photoanode exhibited a smaller arc diameter, and 0.01 M ZnO had a larger arc diameter than all the synthesized photoanodes, which can be assigned as the best and proper photoanodes for effective charge dissociation. For any morphology, an

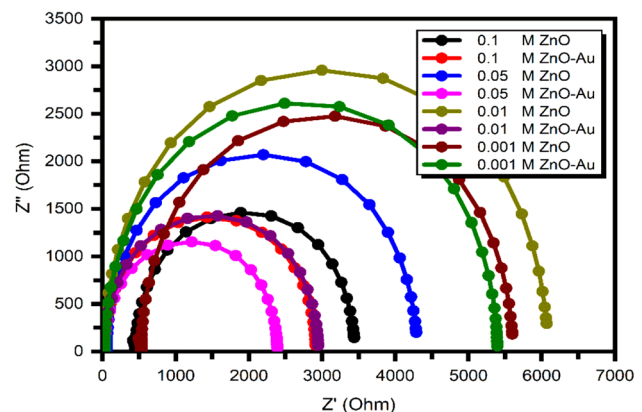


Fig. 9 Nyquist plots of the photoelectrochemical impedance spectra of the synthesized photoanodes

Au-loaded sample shows a smaller arc diameter, interpreting the role of Au plasmons in preventing charge recombination.

4 Conclusions

ZnO thin films with different structures and Au-loaded plasmons on these structures were successfully synthesized on FTO substrate by electrochemical method. The structural parameters from XRD support the morphological analysis obtained from SEM. The ZnO photoanodes have a hexagonal wurtzite structure with a crystal size of ~ 30 nm. The surface area plays a crucial role in the water-splitting mechanism. The deduced results from UV–Visible spectra indicate that the absorption edge has been shifted from the UV region toward the visible region after incorporating Au plasmons, thereby exhibiting a high rate of light captivation in the visible region by Au plasmons. The band gap values are ~ 3.15 eV for all the concentrations. A similar result was observed from PL measurement. The intensity of the emission spectra has been enhanced for 0.05 M ZnO–Au photoanode, showing lower defect states present due to sheet morphology. However, the pristine 0.1 M ZnO photoanode exhibited better optical properties than the 0.05 M ZnO–Au photoanode. The obtained results from the utilized characterizations indicate that the 0.05 M ZnO–Au photoanode is a better candidate for the PEC splitting of water, exhibiting maximum photocurrent conversion efficiency (0.38%) and the highest photocurrent density (0.69 mA/cm²) among synthesized photoanodes. The active surface area changes depending on the morphology; thus, a higher surface area gives better water-splitting results. ZnO nanostructures-based photoanodes modified with plasmons can be a prospective candidate for efficient PEC cells.

Acknowledgements

Shruti Shah, Vidya Doiphode, Pratibha Shinde, Ashish Waghmare, Yogesh Hase, and Bharat Bade are grateful to the Ministry of New and Renewable Energy (MNRE), Government of India New Delhi, for the National Renewable Energy (NRE) fellowship and financial assistance. Ashvini Punde is thankful to the Mahatma Jyotiba Phule Research and Training Institute (MAHAJYOTI), Government of Maharashtra,

for the Mahatma Jyotiba Phule Research Fellowship (MJPRF). Swati Rahane is thankful for the research fellowship to the Chhatrapati Shahu Maharaj Research, Training and Human Development Institute (SARTHI), Government of Maharashtra. In addition, Vidhika Sharma, and Sandesh Jadkar are thankful to the Indo-French Centre for the Promotion of Advanced Research-CEFIPRA, Department of Science and Technology, New Delhi, for special financial support.

Author contributions

ELD contributed toward methodology, formal analysis, investigation, data curation, and writing-original draft. SM contributed toward formal analysis and data curation. SS contributed toward methodology, validation, formal analysis, and investigation. VS contributed toward formal analysis, data curation, and writing-original draft. BB contributed toward conceptualization, validation, formal analysis, and investigation. SR: contributed toward data curation, formal analysis, and investigation. VD contributed toward methodology, validation, formal analysis, and investigation. PS contributed toward conceptualization, validation, formal analysis, and investigation. AW contributed toward methodology, formal analysis, investigation, and data curation. YH contributed toward methodology, conceptualization, validation, formal analysis, and investigation. AP contributed toward methodology, validation, formal analysis, and investigation. SL contributed toward data curation, formal analysis, and investigation. MP contributed toward data curation, writing-review, and editing. SJ contributed toward visualization, writing-review, editing, supervision, and funding acquisition.

Data availability

The datasets used and analyzed during the current study are available from the corresponding author upon reasonable request.

Declarations

Competing interests The authors declare that they have no known competing financial interests or per-

sonal relationships that could have appeared to influence the work reported in this paper.

References

1. P. Shinde, V. Sharma, A. Punde, A. Waghmare, P. Vairale, Y. Hase, S. Pandharkar, A. Bhorde, R. Aher, S. Nair, V. Doiphode, V. Jadkar, N. Patil, S. Rondiya, M. Prasad, S. Jadkar, 2D alignment of zinc oxide@ZIF8 nanocrystals for photoelectrochemical water splitting. *New J. Chem.* **45**, 3498–3507 (2021). <https://doi.org/10.1039/D0NJ05567K>
2. S. Sharma, S. Singh, N. Khare, Enhanced photosensitization of zinc oxide nanorods using polyaniline for efficient photocatalytic and photoelectrochemical water splitting. *Int. J. Hydrogen Energy* **41**, 21088–21098 (2016). <https://doi.org/10.1016/j.ijhydene.2016.08.131>
3. Y. Yang, S. Niu, D. Han, T. Liu, G. Wang, Y. Li, Progress in developing metal oxide nanomaterials for photoelectrochemical water splitting. *Adv. Energy Mater.* **7**, 1700555 (2017). <https://doi.org/10.1002/aenm.201700555>
4. P. Subramanyam, B. Meena, V. Biju, H. Misawa, S. Chalalalli, Emerging materials for plasmon-assisted photoelectrochemical water splitting. *J. Photochem. Photobiol. C Photochem. Rev.* **51**, 100472 (2022). <https://doi.org/10.1016/j.jphotochemrev.2021.100472>
5. A. Fujishima, K. Honda, Electrochemical photolysis of water at a semiconductor electrode. *Nature* **238**, 3738 (1972). <https://doi.org/10.1038/238037a0>
6. J. Han, Z. Liu, Optimization and modulation strategies of zinc oxide-based photoanodes for highly efficient photoelectrochemical water splitting. *ACS Appl. Energy Mater.* **4**, 1004–1013 (2021). <https://doi.org/10.1021/acsaem.0c02985>
7. M. Liu, C.Y. Nam, C.T. Black, J. Kamcev, L. Zhang, Enhancing water splitting activity and chemical stability of zinc oxide nanowire photoanodes with ultrathin titania shells. *J. Phys. Chem. C* **117**, 13396–13402 (2013). <https://doi.org/10.1021/jp404032p>
8. S. Shet, Y. Yan, H. Wang, N. Ravindra, J. Turner, M. Al Jassim, Synthesis of ZnO nanostructures and their influence on photoelectrochemical response for solar driven water splitting to produce hydrogen. *Advances and applications in electroceramics II-materials science and technology. Adv. Nanomater. Nanostruct.* **229**, 231 (2012). <https://doi.org/10.1002/9781118144602.ch14>
9. A.K. Chandiran, M. Abdi-Jalebi, M.K. Nazeeruddin, M. Grätzel, Analysis of electron transfer properties of ZnO and TiO₂ photoanodes for dye-sensitized solar cells. *ACS Nano* **8**, 2261–2268 (2014). <https://doi.org/10.1021/nn405535j>
10. C. Li, S. Chen, Y. Wang, Z. Hou, ZnO/ZnS heterostructures grown on Zn foil substrate by hydrothermal method for photoelectrochemical water splitting. *Int. J. Hydrogen Energy* **44**, 25416–25427 (2019). <https://doi.org/10.1016/j.ijhydene.2019.07.206>
11. C. Cheng, K.R. Gustavsen, K. Wang, Plasmon-induced visible light absorption arising from edge-interfaces of titanium-oxides nanocomposites. *Opt. Mater.* **113**, 110847 (2021). <https://doi.org/10.1016/j.optmat.2021.110847>
12. M.Z. Iqbal, S. Siddique, Recent progress in efficiency of hydrogen evolution process based photoelectrochemical cell. *Int. J. Hydrogen Energy* **43**, 21502–21523 (2018). <https://doi.org/10.1016/j.ijhydene.2018.09.157>
13. S. Cho, J.W. Jang, K.H. Lee, J.S. Lee, Research update: strategies for efficient photoelectrochemical water splitting using metal oxide photoanodes. *APL Mater.* **2**, 010703 (2014). <https://doi.org/10.1063/1.4861798>
14. Y. Liu, X. Yan, Z. Kang, Y. Li, Y. Shen, Y. Sun, L. Wang, Y. Zhang, Synergistic effect of surface plasmonic particles and surface passivation layer on ZnO nanorods array for improved photoelectrochemical water splitting. *Sci. Rep.* **6**, 29907 (2016). <https://doi.org/10.1038/srep29907>
15. M. Prasad, V. Sharma, R. Aher, A. Rokade, P. Ilaiyaraja, C. Sudakar, S. Jadkar, Synergistic effect of Ag plasmon- and reduced graphene oxide-embedded ZnO nanorod-based photoanodes for enhanced photoelectrochemical activity. *J. Mater. Sci.* **52**, 13572–13585 (2017). <https://doi.org/10.1007/s10853-017-1436-4>
16. H. Li, Z. Li, Y. Yu, Y. Ma, W. Yang, F. Wang, X. Yin, X. Wang, Surface-plasmon-resonance-enhanced photoelectrochemical water splitting from Au-nanoparticle-decorated 3D TiO₂ nanorod architectures. *J. Phys. Chem. C* **121**, 12071–12079 (2017). <https://doi.org/10.1021/acs.jpcc.7b03566>
17. C. Mahala, M.D. Sharma, M. Basu, Near-field and far-field plasmonic effects of gold nanoparticles decorated on ZnO nanosheets for enhanced solar water splitting. *ACS Appl. Nano Mater.* **3**, 1153–1165 (2020). <https://doi.org/10.1021/acsanm.9b01678>
18. M. Zayed, N. Nasser, M. Shaban, H. Alshaikh, H. Hamdy, A.M. Ahmed, Effect of morphology and plasmonic on Au/ZnO films for efficient photoelectrochemical water splitting. *Nanomaterials* **11**(9), 2338 (2021). <https://doi.org/10.3390/nano11092338>
19. S.A. Saboor, V. Sharma, E.L. Darboe, V. Doiphode, A. Punde, P. Shinde, V. Jadkar, Y. Hase, A. Waghmare, M. Prasad, S. Jadkar, Influence of Au plasmons and their synergistic effects with ZnO nanorods for photoelectrochemical

- water splitting applications. *J. Mater. Sci. Mater. Electron.* **32**, 20525–20538 (2021). <https://doi.org/10.1007/s10854-021-06564-4>
20. H. Li, H. Liu, F. Wang, G. Li, X. Wang, Z. Tang, Hot electron assisted photoelectrochemical water splitting from Au-decorated ZnO@TiO₂ nanorods array. *Nano Res.* **15**, 5824–5830 (2022). <https://doi.org/10.1007/s12274-022-4203-z>
 21. M. Wu, W.J. Chen, Y.H. Shen, F.Z. Huang, C.H. Li, S.K. Li, In situ growth of matchlike ZnO/Au plasmonic heterostructure for enhanced photoelectrochemical water splitting. *ACS Appl. Mater. Interfaces* **6**, 15052–15060 (2014). <https://doi.org/10.1021/am503044f>
 22. Z. Yan, H. Liu, Z. Hao, M. Yu, X. Chen, J. Chen, Electrodeposition of (hydro)oxides for an oxygen evolution electrode. *Chem. Sci.* **11**, 10614–10625 (2020). <https://doi.org/10.1039/D0SC01532F>
 23. C. Chang, S. Zhu, X. Liu, Y. Chen, Y. Sun, Y. Tang, P. Wan, J. Pan, One-step electrodeposition synthesis of bimetal Fe- and co-doped NiPi/P for highly efficient overall water splitting. *Ind. Eng. Chem. Res.* **60**, 2070–2078 (2021). <https://doi.org/10.1021/acs.iecr.0c05365>
 24. M. Zayed, N. Nasser, M. Shaban, H. Alshaikh, H. Hamdy, A.M. Ahmed, Effect of morphology and plasmonic on Au/ZnO films for efficient photoelectrochemical water splitting. *Nanomaterials* **1**(9), 2338–19 (2021). <https://doi.org/10.3390/nano11092338>
 25. X. Zheng, Z. Zhang, S. Meng, Y. Wang, D. Li, Regulating charge transfer over 3D Au/ZnO hybrid inverse opal toward efficiently photocatalytic degradation of bisphenol A and photoelectrochemical water splitting. *Chem. Eng. J. s* **393**, 124676 (2020). <https://doi.org/10.1016/j.cej.2020.124676>
 26. A.C. Guler, J. Antoš, M. Masař, M. Urbánek, M. Machovský, I. Kuřitka, Boosting the photoelectrochemical performance of Au/ZnO nanorods by co-occurring gradient doping and surface plasmon modification. *Int. J. Mol. Sci.* **24**(1), 443 (2022). <https://doi.org/10.3390/ijms24010443>
 27. X. Shao, B. Li, B. Zhang, L. Shao, Y. Wu, Au@ ZnO core-shell nanostructures with plasmon-induced visible-light photocatalytic and photoelectrochemical properties. *Inorg. Chem. Front.* **3**(7), 934–943 (2016). <https://doi.org/10.1039/C6QI00064A>
 28. W. Zhang, W. Wang, H. Shi, Y. Liang, J. Fu, M. Zhu, Surface plasmon-driven photoelectrochemical water splitting of aligned ZnO nanorod arrays decorated with loading-controllable Au nanoparticles. *Sol. Energy Mater. Sol. Cells* **180**, 25–33 (2018). <https://doi.org/10.1016/j.solmat.2018.02.020>
 29. P. Muhammed Shafi, A. Chandra Bose, Impact of crystalline defects and size on X-ray line broadening: a phenomenological approach for tetragonal SnO₂ nanocrystals. *AIP Adv.* **5**, 057137 (2015). <https://doi.org/10.1063/1.4921452>
 30. A.R. Marlinda, N. Yusoff, A. Pandikumar, N.M. Huang, O. Akbarzadeh, S. Sagadevan, Y.A. Wahab, M.R. Johan, Tailoring morphological characteristics of zinc oxide using a one-step hydrothermal method for photoelectrochemical water splitting application. *Int. J. Hydrogen Energy* **44**, 17535–17543 (2019). <https://doi.org/10.1016/j.ijhydene.2019.05.109>
 31. K.R. Nandanapalli, D. Mudusu, J.S. Yu, S. Lee, Stable and sustainable photoanodes using zinc oxide and cobalt oxide chemically gradient nanostructures for water-splitting applications. *J. Colloid Interface Sci.* **558**, 9–20 (2020). <https://doi.org/10.1016/j.jcis.2019.09.086>
 32. P.J. Scherrer, Estimation of the size and internal structure of colloidal particles by means of röntgen. *Nachr. Ges. Wiss. Göttingen.* **2**, 96–100 (1918)
 33. J.I. Langford, A.J. Wilson, Scherrer after sixty years: a survey and some new results in the determination of crystallite size. *J. Appl. Crystallogr.* **11**(2), 102–113 (1978). <https://doi.org/10.1107/S0021889878012844>
 34. V.L. Uvarov, I. Popov, Metrological characterization of X-ray diffraction methods for determination of crystallite size in nano-scale materials. *Mater. Charact.* **58**(10), 883–91 (2007). <https://doi.org/10.1016/j.matchar.2006.09.002>
 35. G.K. Williamson, W.H. Hall, X-ray line broadening from filed aluminium and wolfram. *Acta Metall.* **1**(1), 22–31 (1953). [https://doi.org/10.1016/0001-6160\(53\)90006-6](https://doi.org/10.1016/0001-6160(53)90006-6)
 36. X.D. Zhang, P. Wu, Y.Y. Shen, L.H. Zhang, Y.H. Xue, F. Zhu, D.C. Zhang, Liu CL (2011) Structural and optical properties of Au-implanted ZnO films. *Appl. Surf. Sci.* **258**(1), 151–157 (2011). <https://doi.org/10.1016/j.apsusc.2011.08.022>
 37. B. Yahmadi, N. Kamoun, C. Guasch, Bennaceur R (2011) Synthesis and characterization of nanocrystallized In₂S₃ thin films via CBD technique. *Mater. Chem. Phys.* **127**(1–2), 239–247 (2011). <https://doi.org/10.1016/j.matchemphys.2011.01.066>
 38. A. Janotti, C.G. Van De Walle, Oxygen vacancies in ZnO. *Appl. Phys. Lett.* **87**, 122102 (2005). <https://doi.org/10.1063/1.2053360>
 39. S. Fiedler, L.O. Lee Cheong Lem, C. Ton That, A. Hoffmann, M.R. Phillips, Enhancement of the UV emission from gold/ZnO nanorods exhibiting no green luminescence. *Opt. Mater. Express* **10**, 1476–1487 (2020). <https://doi.org/10.1364/OME.381527>

40. F. Rasouli, A. Rouhollahi, F. Ghahramanifard, Gradient doping of copper in ZnO nanorod photoanode by electro-deposition for enhanced charge separation in photoelectrochemical water splitting. *Superlattices Microstruct.* **125**, 177–189 (2019). <https://doi.org/10.1016/j.spmi.2018.08.026>
41. P.P. Patel, P.J. Hanumantha, O.I. Velikokhatnyi, M.K. Datta, D. Hong, B. Gattu, J.A. Poston, A. Manivannan, P.N. Kumta, Nitrogen and cobalt co-doped zinc oxide nanowires—viable photoanodes for hydrogen generation via photoelectrochemical water splitting. *J. Power. Sources* **299**, 11–24 (2015). <https://doi.org/10.1016/j.jpowsour.2015.08.027>
42. N.S.K. Gowthaman, J.W. Chen, C.F. Dee, S.P. Chai, W.S. Chang, Nanostructural dimension and oxygen vacancy synergistically induced photoactivity across high surface area monodispersed AuNPs/ZnO nanorods heterojunction. *J. Alloys Compd.* **920**, 165836 (2022). <https://doi.org/10.1016/j.jallcom.2022.165836>
43. A. Machín, M. Cotto, J. Duconge, J.C. Arango, C. Morant, S. Pinilla, V.L. Soto, E. Resto, F. Márquez, Hydrogen production via water splitting using different Au@ZnO catalysts under UV-vis irradiation. *J. Photochem. Photobiol. A* **353**, 385–394 (2018). <https://doi.org/10.1016/j.jphotochem.2017.11.050>
44. H.M. Chen, C.K. Chen, C.J. Chen, L.C. Cheng, P.C. Wu, B.H. Cheng, Y.Z. Ho, M.L. Tseng, Y.Y. Hsu, T.S. Chan, J.F. Lee, R.S. Liu, D.P. Tsai, Plasmon inducing effects for enhanced photoelectrochemical water splitting: X-ray absorption approach to electronic structures. *ACS Nano* **6**, 7362–7372 (2012). <https://doi.org/10.1021/nn3024877>
45. A. Wolcott, W.A. Smith, T.R. Kuykendall, Y. Zhao, J.Z. Zhang, Photoelectrochemical study of nanostructured ZnO thin films for hydrogen generation from water splitting. *Adv. Funct. Mater.* **19**, 1849–1856 (2009). <https://doi.org/10.1002/adfm.200801363>
46. C.F. Windisch, G.J. Exarhos, Mott-Schottky analysis of thin ZnO films. *J. Vac. Sci. Technol. A* **18**, 1677 (2000). <https://doi.org/10.1116/1.582406>
47. A. Ahmadi, M. Zargar Shoushtari, Enhancing the photoelectrochemical water splitting performance of WS2 nanosheets by doping titanium and molybdenum via a low-temperature CVD method. *J. Electroanal. Chem.* **849**, 113361 (2019). <https://doi.org/10.1016/j.jelechem.2019.113361>
48. K. Gelderman, L. Lee, S.W. Donne, Flat-band potential of a semiconductor: using the Mott-Schottky equation. *J. Chem. Educ.* **84**, 685 (2007). <https://doi.org/10.1021/ed084p685>
49. C. Poole, I. Darwazeh, *Microwave Semiconductor Materials and Diodes Microwave Active Circuit Analysis and Design*, pp. 355 (Elsevier, Amsterdam, 2016). ISBN: 8120324188, 9788120324183
50. R.B. Wei, P.Y. Kuang, H. Cheng, Y.B. Chen, J.Y. Long, M.Y. Zhang, Z.Q. Liu, Plasmon-enhanced photoelectrochemical water splitting on gold nanoparticle decorated ZnO/CdS nanotube arrays. *ACS Sustain. Chem. Eng.* **5**, 4249–4257 (2017). <https://doi.org/10.1021/acssuschemeng.7b00242>

Publisher's Note Springer Nature remains neutral with regard to jurisdictional claims in published maps and institutional affiliations.

Springer Nature or its licensor (e.g. a society or other partner) holds exclusive rights to this article under a publishing agreement with the author(s) or other rightsholder(s); author self-archiving of the accepted manuscript version of this article is solely governed by the terms of such publishing agreement and applicable law.